

# CycleGAN with a Blur Kernel for Deconvolution Microscopy: Optimal Transport Geometry

Sungjun Lim<sup>1</sup>, Sang-Eun Lee<sup>2</sup>, Sunghoe Chang<sup>2</sup>, Byeongsu Sim<sup>3</sup>, and Jong Chul Ye<sup>1</sup>, *Senior Member, IEEE*

**Abstract**—Deconvolution microscopy has been extensively used to improve the resolution of the widefield fluorescent microscopy. However, classical deconvolution approaches require the measurement or estimation of the point spread function (PSF), and are computationally expensive. Recently, convolutional neural network (CNN) approaches have been extensively studied as fast and high performance alternatives. Unfortunately, the CNN approaches usually require matched high resolution images for supervised training. In this paper, we present a novel *unsupervised* cycle-consistent generative adversarial network (cycleGAN) with a linear blur kernel, which can be used for both blind- and non-blind image deconvolution. In contrast to the conventional cycleGAN approaches that require two generators, the proposed cycleGAN approach needs only a single generator, which significantly improves the robustness of network training. We show that the proposed architecture is indeed a dual formulation of an optimal transport problem that uses a special form of penalized least squares as transport cost. Experimental results using simulated and real experimental data confirm the efficacy of the algorithm.

**Index Terms**—Deconvolution microscopy, unsupervised learning, generative adversarial network (GAN), cycle consistency, optimal transport, penalized least squares

## I. INTRODUCTION

**L**ight diffraction from a given optics limits the resolution of images, creating blur and haze which degrade fine details of the intracellular organelles. Therefore, deconvolution techniques are usually required to improve the resolution [1].

Mathematically, a blurred image  $g(\mathbf{r})$  can be represented as a convolution between an unobserved object  $x(\mathbf{r})$  and a 3D point-spread function (PSF)  $h(\mathbf{r})$ :

$$\begin{aligned} g(\mathbf{r}) &= h * x(\mathbf{r}) \\ &= \int_{\mathbb{R}^3} h(\mathbf{r} - \mathbf{r}') x(\mathbf{r}') d\mathbf{r}', \quad \mathbf{r} \in \mathbb{R}^3. \end{aligned} \quad (1)$$

which is also corrupted by noises:

$$y = h * x + w, \quad (2)$$

where  $w$  is the measurement noise.

It is well-known that a deconvolution microscopy problem, which obtains  $x$  from the sensor measurement  $y$ , is ill-posed. A standard strategy to address the ill-posed inverse problems is a penalized least squares approach to stabilize the solution:

$$\min_x \|y - h * x\|^q + R(x) \quad (3)$$

for  $q \geq 1$ , where  $R(x)$  is a regularization (or penalty) function such as  $l_1$ , total variation (TV), etc [1]–[3]. The reason to use a general  $q$  value instead of the standard choice of  $q = 2$  will soon become clear.

If the PSF  $h(\mathbf{r})$  is not known, which is often referred to as the blind deconvolution problem, both the unknown PSF  $h(\mathbf{r})$  and the image  $x(\mathbf{r})$  should be estimated. For example, the authors in [4], [5] proposed a blind deconvolution method by solving a joint minimization problem to estimate both the unknown blur kernel and the image by adding additional penalty (such as  $l_1$  or total variation (TV)) for the unknown blur kernel:

$$\min_{x, h} \|y - h * x\|^q + R(x) + Q(h) \quad (4)$$

where  $Q(h)$  is the regularization term for the blur kernel. For the sake of simplicity, we consider (4) to be the most general form of the penalized least squares formulation for deconvolution microscopy, since the non-blind case becomes a special case by setting  $Q(h) = \chi_{h^*}(h)$ , where  $\chi_{h^*}(\cdot)$  is the indicator function for the ground-truth PSF  $h^*$ .

Recently, convolutional neural networks (CNN) have been extensively investigated to enhance the resolution of optical microscopy. Rivenson et al. [6] used deep neural networks to enhance its spatial resolution for a large field-of-view and depth-of-focus optical microscopy. Nehme et al. [7] used a deep convolutional neural network to obtain super resolution images from localization microscopy. Weigert et al. [8] proposed a CNN method which can recover isotropic resolution from anisotropic data. Zelger et al. [9] used a CNN method to localize particles in three dimensions from a single image. In these works, the neural networks are usually trained in a supervised manner, necessitating high resolution reference images that are matched to each low resolution images.

Recently, generative adversarial network (GAN) has attracted significant attention in inverse problems by providing a way to use unmatched data to train a deep neural network [10]. In particular, the authors in [11] proposed so-called Wasserstein GAN, which is closely related to the mathematical theory of optimal transport [12], [13]. For microscopy applications, Nguyen et al. [14] developed a novel CNN framework with conditional generative adversarial network (cGAN) framework to reconstruct video sequences of dynamic live cells from Fourier ptychographic microscopy (FPM). Kupyn et al. [15] proposed the so-called DeblurGAN for motion deblurring with a conditional GAN and content loss. Unfortunately, these GAN approaches often generate artificial features due to the mode collapsing, so a cycle-consistent

SL and JCY are with the Department of Bio and Brain Engineering, Korea Advanced Institute of Science and Technology (KAIST), Daejeon 34141, Republic of Korea (e-mail: {jong.ye}@kaist.ac.kr). BS and JCY are with the Dept. of Mathematical Sciences, KAIST. SEL and SC are with the Department of Physiology & Biomedical Sciences, Seoul National University College of Medicine, Seoul 03080, Republic of Korea.

adversarial network (CycleGAN) [16] that imposes the one-to-one correspondence has been extensively investigated for image reconstruction [17], [18]. However, cycleGAN training is relatively difficult as two deep generators should be trained simultaneously.

One of the most important contributions of this paper is, therefore, to show that the cycleGAN architecture with two generators may not be necessary for unsupervised deconvolution microscopy. Instead, a simple linear blur generator may be sufficient to generate low resolution images, thereby reducing the required number of CNN generators to only one. This makes the training much easier and more stable compared to the original cycleGAN approaches with two deep generators. Another important contribution of this paper is to reveal the theoretical background for the success of the new architecture, i.e. our cycleGAN architecture is indeed a dual formulation of the optimal transport problem [12], [13] when the penalized least squares formulation (3) with the deep learning penalty is used as a transport cost between the two measures. Recall that the optimal transport problem is to compare two measures in a Lagrangian framework [12], [13]. The use of the optimal transport theory is suitable for the unsupervised deconvolution problem, since it can utilize the unmatched high resolution image data to stabilize the deconvolution solution. Thanks to the Kantorovich dual formulation [12], [13], we show that the optimal transport problem can be implemented by the proposed cycleGAN with a linear blur kernel.

This paper is composed as follows. In Section II, we provide a review of necessary mathematical preliminaries. Section III then proposes a cycleGAN architecture with a linear blur kernel as a dual formulation of the optimal transport problem with the penalized least squares. The network implementation is detailed in Section IV. The experimental methods and results are provided in Section V and Section VI, respectively, which are followed by the conclusion in Section VII.

## II. RELATED WORKS

### A. Optimal Transport

In this section, we provide a brief review of the optimal transport theory to make the paper self-contained.

Optimal transport theory [12], [13] gives a mathematical framework that makes it possible to measure distances between two measures. In optimal transport theory, both measures are usually considered as probability measures supported on the  $\mathcal{X}$  and  $\mathcal{Y}$  spaces, respectively, i.e.  $\mu \in P(\mathcal{X})$  and  $\nu \in P(\mathcal{Y})$ . Let  $c : \mathcal{X} \times \mathcal{Y} \mapsto [0, \infty]$  be a transport cost where  $c(x, y)$  measures the expense of transporting one unit of mass  $x \in \mathcal{X}$  to  $y \in \mathcal{Y}$ . Essentially one pays a cost for transporting one measure to another, so that the similarity of the two measures are quantified using the minimum transportation cost for transporting one measure to another. Formally, we say that  $T : \mathcal{X} \mapsto \mathcal{Y}$  transports  $\mu \in P(\mathcal{X})$  to  $\nu \in P(\mathcal{Y})$ , if

$$\nu(B) = \mu(T^{-1}(B)), \quad \text{for all } \nu\text{-measureable set } B, \quad (5)$$

which condition is often simply represented by

$$\nu = T_{\#}\mu, \quad (6)$$

where  $T_{\#}$  is often called the push-forward operator. Then, Monge's original optimal transport problem [12], [13] is to find a transport map  $T$  that transport  $\mu$  to  $\nu$  at the minimum total transportation cost, which can be formulated as

$$\begin{aligned} \min_T \quad & \mathbb{M}(T) := \int_{\mathcal{X}} c(x, T(x)) d\mu(x) \\ \text{subject to} \quad & \nu = T_{\#}\mu \end{aligned} \quad (7)$$

However, Monge's original formulation usually requires combinatorial approaches due to the nature of deterministic assignment. Kantorovich relaxed the assumption to consider a probabilistic transport, which allows mass splitting from a source toward several targets [12], [13]. Specifically, Kantorovich introduced a joint measure  $\pi \in P(\mathcal{X} \times \mathcal{Y})$  and the associated cost  $c(x, y), x \in \mathcal{X}, y \in \mathcal{Y}$  such that  $d\pi(x, y)$  becomes the amount of mass transferred from  $x$  to  $y$  and  $c(x, y)d\pi(x, y)$  is the associated cost. Accordingly, mass can be transferred from  $x$  to multiple locations. Then, the Kantorovich's formulation of the optimal transport problem is defined as

$$\begin{aligned} \min_{\pi} \quad & \mathbb{K}(\pi) := \int_{\mathcal{X} \times \mathcal{Y}} c(x, y) d\pi(x, y) \\ \text{subject to} \quad & \pi(A \times \mathcal{Y}) = \mu(A) \\ & \pi(\mathcal{X} \times B) = \nu(B) \end{aligned} \quad (8)$$

for all measurable set  $A \in \mathcal{X}$  and  $B \in \mathcal{Y}$ . Here, the last two constraints come from the observation that the total amount of mass removed from any measurable set has to equal to the marginals [12], [13]. Under some regularity conditions that can be found in [12], [13], we have  $\inf_{\pi} \mathbb{K}(\pi) = \inf_T \mathbb{M}(T)$ , thereby justifying the use of Kantorovich formulation.

Another important advantage of Kantorovich formulation is the dual formulation. Specifically, the dual Kantorovich formulation is given by

$$\begin{aligned} \max_{\varphi, \psi} \quad & \mathbb{J}(\varphi, \psi) := \int_{\mathcal{X}} \varphi d\mu + \int_{\mathcal{Y}} \psi d\nu \\ \text{subject to} \quad & \varphi(x) + \psi(y) \leq c(x, y) \end{aligned} \quad (9)$$

which can be equivalently represented as

$$\max_{\varphi} \quad \int_{\mathcal{X}} \varphi d\mu + \int_{\mathcal{Y}} \varphi^c d\nu \quad (10)$$

where  $\varphi$  is often called the *Kantorovich potential* and  $\varphi^c$  is its *c-transform* defined as

$$\varphi^c(y) := \inf_x c(x, y) - \varphi(x) \quad (11)$$

Again, under some regularity conditions that can be found in [12], [13], we have

$$\max_{\varphi, \psi} \mathbb{J}(\varphi, \psi) = \min_{\pi} \mathbb{K}(\pi).$$

Finally, the Wasserstein distance  $d_{W^p}(\mu, \nu)$  between the two measures  $\mu, \nu$  is defined as

$$d_{W^p}(\mu, \nu) = \left( \min_{\pi} \mathbb{K}(\pi) \right)^{\frac{1}{p}} \quad (12)$$

when one choose  $c(x, y) = \|x - y\|^p$  with  $p \geq 1$  in (8).

### B. Learning with Wasserstein Loss

Recently, Adler et al [19] proposed a learning scheme using the miss-aligned training data. Their work was motivated from inverse problems, where the ground-truth label data is scarce and many of the reference data is misaligned by geometric transforms. Since the standard  $l_2$  loss for the supervised training with the misaligned data gives a smeared reconstruction, they employed the Wasserstein distance that correctly compensates for miss-alignments in certain cases [19].

Specifically, for a given forward problem (2), they first define an inversion operator  $G_\Theta$  using a neural network with the parameter  $\Theta$  such that the estimate of the unknown  $x$  is given by  $\tilde{x}_\Theta = G_\Theta(y)$ . After discretizing the reconstructed image and the geometrically misaligned reference, the two measures are defined by point masses on the discretization grid. Then, the neural network is trained to minimize the Wasserstein loss between the two point masses. Adler et al [19] demonstrated that the training with the Wasserstein loss can lead to less blurry reconstruction.

## III. MAIN CONTRIBUTION

### A. Penalized Least Squares for Optimal Transport

One of our most important observations in this paper is that the Wasserstein loss in Adler et al [19], defined as the point masses on the discretization grid, may limit its potential in the use of unmatched reference data. In particular, their “misaligned” reference data for the training should come from similar images to the ground-truth up to the geometric transform. However, in most of the deconvolution microscopy problems, even these “mis-aligned” reference data may not be available; instead, high resolution images from additional algorithms or modalities may be available for different samples.

Another important observation is that the statistical properties of the high and low resolution images are different thanks to the blur kernel, which can be exploited by extending the original idea of Adler et al [19]. For example, suppose that the ground-truth image  $x$  is from the i.i.d Gaussian distribution, i.e  $x \sim \mathcal{N}(0, \sigma_x^2 I)$ , which is the normal distribution with zero mean and covariance  $\sigma_x^2 I$ , where  $I$  is the identity matrix. With the additive noise  $w \sim \mathcal{N}(0, \sigma_w^2 I)$ , the measurement  $y$  in (2) is then distributed by

$$y \sim \mathcal{N}(0, \sigma_w^2 I + \sigma_x^2 (H^\top H))$$

where  $H$  is the convolution matrix given by  $h * x = Hx$ . In deconvolution problems, the ill-posedness of the inverse problem comes from small singular values of  $H$ , which makes the covariance matrix  $\sigma_w^2 I + \sigma_x^2 (H^\top H)$  severely elongated to specific directions. An exemplary geometric view is shown in Fig. 1, where the measurement manifold  $\mathcal{Y}$  for the blurry images are more elongated compared to the high resolution image manifold  $\mathcal{X}$ . Therefore, if the inversion of (2) is correctly done, the reconstructed image  $G_\Theta(y)$  should closely follow the distribution of the high resolution images. Accordingly, instead of using the point mass in the discretization grid as in Adler et al [19], our measures  $\mu, \nu$  are now defined in the space of high resolution images  $\mathcal{X}$  and the low resolution measurement

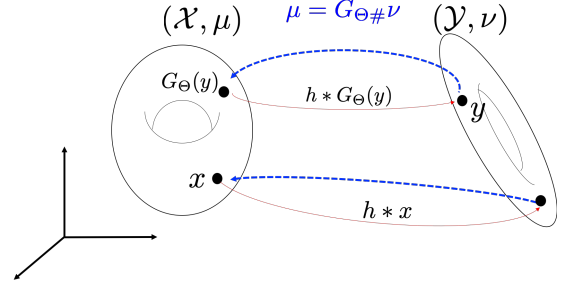


Fig. 1: An example of manifolds  $\mathcal{X}$  and  $\mathcal{Y}$  and their measures  $\mu$  and  $\nu$ , respectively. Due to the blur kernel, the measurement manifold  $\mathcal{Y}$  is more elongated than the high resolution image manifold  $\mathcal{X}$ .

$y \in \mathcal{Y}$ , respectively. This observation leads to the following cost function for the penalized least squares formulation in (4):

$$c(x, y; \Theta, h) = \|y - h * x\|^q + \|G_\Theta(y) - x\|^p + Q(h) \quad (13)$$

for  $p \geq 1$ , which use the distance between the neural network output  $G_\Theta(y)$  and  $x$  as a penalty term to stabilize the solution. Similar form of the penalized least squares have been investigated in deep learning image prior [20], model-based deep learning (MoDL) [21], etc.

However, in contrast to the conventional penalized least squares that first trains a neural network  $G_\Theta(y)$  in a supervised manner and then minimizes the cost (13), our innovation comes from the use of (13) as a cost for transporting mass  $x \in \mathcal{X}$  to  $y \in \mathcal{Y}$ . This is because we do not have reference data to train the neural network, so the direct minimization of the penalized least squares (13) leads to a biased estimation. Instead, we want to find the network parameters that minimize the average transportation cost with respect to the joint measure, i.e. all the combinations of  $x \in \mathcal{X}$  and  $y \in \mathcal{Y}$  for a given joint probability distribution. Specifically, we find the parameters  $\Theta$  and  $h$  such that the following total transportation cost between two measures supported on  $\mathcal{X}$  and  $\mathcal{Y}$  is minimized:

$$\min_{\Theta, h} \mathbb{T}(\Theta, h) := \min_{\pi} \int_{\mathcal{X} \times \mathcal{Y}} c(x, y; \Theta, h) d\pi(x, y) \quad (14)$$

where  $\pi(x, y)$  is the joint measure and  $c(x, y; \Theta, h)$  is given by (13). The following theorem shows that the transportation cost in (14) has an interesting decomposition.

**Theorem 1.** Suppose we have the following two sets:

$$\begin{aligned} A &:= \{(x, y) \in \mathcal{X} \times \mathcal{Y} \mid x = G_\Theta(y), y \in \mathcal{Y}\}, \\ B &:= \{(x, y) \in \mathcal{X} \times \mathcal{Y} \mid y = h * x, x \in \mathcal{X}\} \end{aligned}$$

where the mapping  $G_\Theta : \mathcal{Y} \mapsto \mathcal{X}$  is single-valued. If  $p = q = 1$  for (13), then the average transportation cost  $\mathbb{T}(\Theta, h)$  in (14) can be represented by

$$\mathbb{T}(\Theta, h) = \ell_{\text{cycle}}(\Theta, h) + \ell_{OT'}(\Theta, h) \quad (15)$$

where

$$\ell_{\text{cycle}}(\Theta, h) = \min_{\pi} \int_{A \cup B} c(x, y; \Theta, h) d\pi(x, y) \quad (16)$$

$$\begin{aligned}
&= \int_{\mathcal{X}} \|x - G_{\Theta}(h * x)\| \rho(x) \mu(dx) \\
&+ \int_{\mathcal{Y}} \|y - h * G_{\Theta}(y)\| \sigma(y) \nu(dy) \quad (17)
\end{aligned}$$

for some measurable function  $\rho$  and  $\sigma$  such that  $0 \leq \rho(x) \leq 1$   $\mu$ -a.e., and  $0 \leq \sigma(y) \leq 1$   $\nu$ -a.e.; and

$$\begin{aligned}
\ell_{OT'}(\Theta, h) &= \min_{\pi} \int_{\mathcal{X} \times \mathcal{Y} \setminus A \cup B} c(x, y; \Theta, h) d\pi(x, y) \quad (18) \\
&= \max_{\varphi} \int_{\mathcal{X}} \varphi(x) d\mu(x) - \int_{\mathcal{Y}} \varphi(G_{\Theta}(y)) d\nu(y) \\
&+ \max_{\psi} \int_{\mathcal{Y}} \psi(y) d\nu(y) - \int_{\mathcal{X}} \psi(h * x) d\mu(x) \quad (19)
\end{aligned}$$

where  $\varphi$  and  $\psi$  are 1-Lipschitz Kantorovich potential functions.

*Proof.* See Appendix. ■

### B. Derivation of CycleGAN with a Single Generator

Note that CycleGAN [16] has been widely used for various unsupervised learning tasks [22]–[24]. Specifically, the authors in [16] are interested in unsupervised translation between the two domains  $\mathcal{X}$  and  $\mathcal{Y}$ . For this, they designed two generators using deep neural networks, where a generator  $G$  maps an image  $y \in \mathcal{Y}$  to  $x \in \mathcal{X}$ , and another generator  $F$  converts an image  $x' \in \mathcal{X}$  to  $y' \in \mathcal{Y}$ . One of the uniqueness of the cycleGAN is that the following cycle-consistency is imposed during the generator training:

$$G \circ F = I, \quad F \circ G = I \quad (20)$$

Furthermore, the discriminator networks  $D_X$  and  $D_Y$  are simultaneously trained to distinguish the synthetically generated images from real ones for each domain so that eventually the synthesized images can follow the probability distributions of real ones. This makes the generators trained to produce more realistic images. For inverse problems, Kang et al [17] employs the cycle-consistent CNN for low-dose cardiac CT denoising without matched low- and high- dose pairs. By augmenting spatial transformer layer, Kim et al [25] extends the architecture to deal with the unsupervised deformable image registration.

Note that if  $\rho(x)$  and  $\sigma(y)$  in (16) is non-zero constant, then the term  $\ell_{cycle}(\Theta, h)$  is indeed similar to the cycle consistency term in cycleGAN [16]. However, our cycle-consistency in (16) imposes the constraint  $x \simeq G_{\Theta}(h * x)$  and  $y \simeq h * G_{\Theta}(y)$ , which requires just one neural network-based generator, whereas the other one can be realized using a convolutional layer with the PSF  $h$ . A geometric view of these constraints is illustrated in Fig. 1. Here, the push-forward operator  $\mu = G_{\Theta\#}\nu$  transports the measure  $\nu$  supported on the blurry image measurement manifold  $\mathcal{Y}$  to the measure  $\mu$  supported on the high resolution image manifold  $\mathcal{X}$ . However, for each  $y \in \mathcal{Y}$  (resp, for each  $x \in \mathcal{X}$ ), the successive application of transport between two spaces, i.e.  $h * G_{\Theta}(y)$  (resp.  $G_{\Theta}(h * x)$ ) should return to the original points  $y$  (resp.  $x$ ).

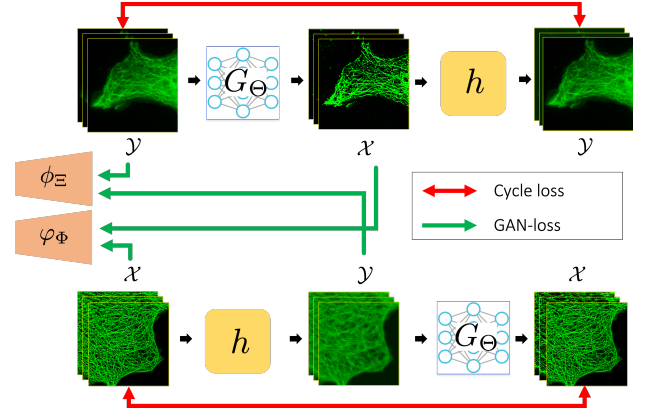


Fig. 2: Proposed cycleGAN architecture with a blur kernel for deconvolution microscopy. Here,  $G_{\Theta}$  denotes the CNN-based low-resolution to high-resolution generator. The blur generator is composed of a linear blur kernel  $h$ . In addition,  $\phi_{\Phi}$  and  $\phi_{\Xi}$  refer to the CNN-based discriminators for the high resolution image domain  $\mathcal{X}$  and the low-resolution image domain  $\mathcal{Y}$ , respectively.

The use of single deep generator makes the cycleGAN training more stable compared to the use of two deep generators.

Now, if we apply the parameterization of the Kantorovich potential as  $\varphi := \varphi_{\Phi}$  and  $\psi := \psi_{\Xi}$  using parameters  $\Phi$  and  $\Xi$ , respectively, then the next term in (15) becomes the following Wasserstein GAN loss function:

$$\ell_{OT'}(\Theta, h) := \max_{\Phi, \Xi} \ell_{GAN}(\Theta, h; \Phi, \Xi)$$

where

$$\begin{aligned}
\ell_{GAN}(\Theta, h; \Phi, \Xi) &= \int_{\mathcal{X}} \varphi_{\Phi}(x) d\mu(x) - \int_{\mathcal{Y}} \varphi_{\Phi}(G_{\Theta}(y)) d\nu(y) \\
&+ \int_{\mathcal{Y}} \psi_{\Xi}(y) d\nu(y) - \int_{\mathcal{X}} \psi_{\Xi}(h * x) d\mu(x) \quad (21)
\end{aligned}$$

Therefore, the minimization of  $\ell_{OT'}(\Theta, h)$  requires competition between  $\varphi_{\Phi}$  and  $G_{\Theta}(y)$ , or between  $\psi_{\Xi}$  and  $h * x$ . This confirms that the Kantorovich potential  $\varphi_{\Phi}$  is the discriminator for the high resolution image domain  $\mathcal{X}$ , whereas  $\psi_{\Xi}$  is the discriminator for the low resolution image domain  $\mathcal{Y}$ .

Finally, by collecting all terms in the transportation cost  $\mathbb{T}(\Theta, h)$  together, we have the following minmax problem:

$$\min_{\Theta, h} \mathbb{T}(\Theta, h) = \min_{\Theta, h} \max_{\Phi, \Xi} \ell(\Theta, h; \Phi, \Xi) \quad (22)$$

where

$$\ell(\Theta, h; \Phi, \Xi) = \ell_{cycle}(\Theta, h) + Q(h) + \ell_{GAN}(\Theta, h; \Phi, \Xi)$$

where  $\ell_{cycle}(\Theta, h)$  denotes the cycle consistent loss in (16) and  $\ell_{GAN}(\Theta, h; \Phi, \Xi)$  is the GAN loss defined in (21). Therefore, the optimization problem (22) can be implemented using a novel cycleGAN architecture with a linear blur kernel as shown in Fig. 2.

#### IV. NETWORK IMPLEMENTATION

##### A. Generator architecture

The network architecture of the high resolution image generator  $G_\Theta$  from the low-resolution image is a modified 3D-Unet [26] as shown in Fig 3. Our U-net structure consists of contracting and expanding paths. The contracting path consists of the repetition of the following blocks: 3D conv-Instance Normalization [27]- ReLU. Here, the generator has symmetric configuration so that both encoder and decoder have the same number of layers, i.e.  $\kappa = 7$ . Throughout the network, the convolutional kernel dimension is  $3 \times 3 \times 3$ . There exists a pooling layer and skipped connection for every other convolution operations. To enhance the image contrast, we add additional sigmoid layer at the end of U-Net.

On the other hand, the low-resolution image generator from high resolution input is based on a single 3D convolution layer that models a 3D blurring kernel. The size of the 3D PSF modeling layer is chosen depending on the problem set by considering their approximate PSF sizes. In this paper, the size of the 3D PSF layer is set to  $10 \times 10 \times 10$  for the simulation study, and  $20 \times 20 \times 20$  for the real experiments, respectively. As for the penalty for the filter for blind deconvolution, we use the  $l_1$  loss, i.e.  $Q(h) = \lambda \|h\|_1$  for some parameter  $\lambda$ .

##### B. Discriminator architecture

Given that our formulation leads to the cycle-consistency loss and Wasserstein GAN loss, we aim at further improving the performance by employing the state-of-the-art GAN loss. Although in this case it is difficult to obtain the close form expression of the original penalized least squares transport cost, empirically we found that such modification improves the reconstruction performance while having a similar theoretical foundation.

Specifically, as for the discriminators, we follow the original CycleGAN that uses multi-PatchGANs (mPGANs) [28], where each discriminator has input patches with different sizes used. As shown in Fig 4, it consist of three independent discriminators. Each discriminator takes patches at different sizes: original, and half, and quarter size patches.

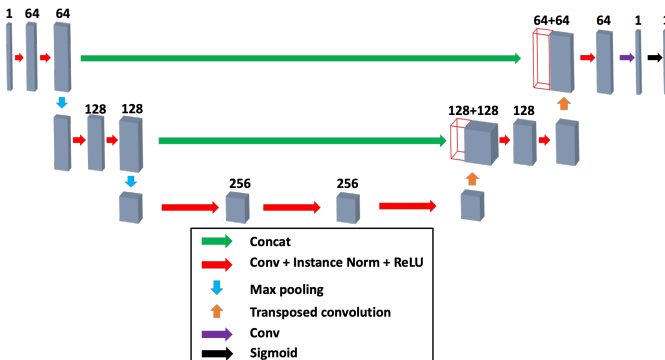


Fig. 3: A modified 3D U-net architecture for our high-resolution image generator.

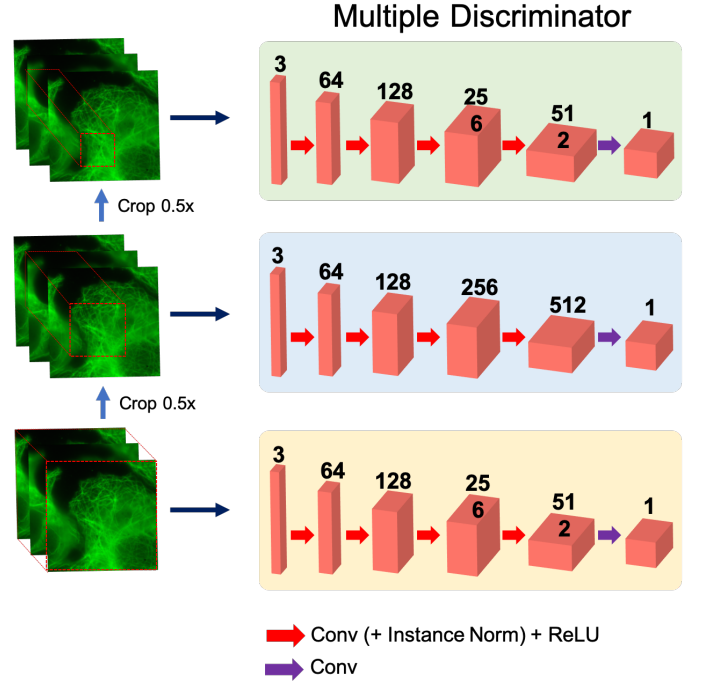


Fig. 4: Multi-PatchGANs discriminator architecture.

#### V. METHOD

##### A. Simulation Study

For simulation studies with the ground-truth data, we used synthetic microtubule network data set [29] to train and validate our model. Specifically, from the ground-truth high resolution synthetic microtubule images, we generate blurred images by convolving them with a model PSF.

In particular, the numerical PSF was computed using the Born and Wolf model [30], which is given by

$$h(r_x, r_y, r_z) =$$

$$\left| C \int_0^1 J_0 \left[ k \frac{NA}{n_i} \rho \sqrt{r_x^2 + r_y^2} \right] e^{-\frac{1}{2} j k \rho^2 r_z \left( \frac{NA}{n_i} \right)^2} \rho d\rho \right|^2 \quad (23)$$

where  $C$  is a normalizing constant,  $k = 2\pi/\lambda$  is the wave number of emitted light,  $\lambda$  is the wavelength,  $NA$  is the numerical aperture, and  $n_i$  is the refractive index of immersion layer. For all simulation, we use  $NA = 1.4$ , and  $n_i = 1.5$ . Then, the simulation is performed with different  $\lambda$  for the PSF model (23). The convolution was performed using DeconvolutionLab2 [29].

The convolved data was then added with the mixture of zero mean Gaussian with the standard deviation  $\sigma = 3$  and Poisson noises with the parameter  $m = 7$ .

The size of the synthetic data was  $256 \times 512 \times 128$ , and 18 samples of the synthetic data were used for training and the other one is used for validation. Due to memory limitations, the volume was split into  $64 \times 64 \times 64$  size patches, which are used as inputs to the neural network.

### B. Real Microscopy Experiments

We also used epifluorescence (EPF) data to validate our model. The samples for our real microscopy experiments are prepared as follows.

1) *Cell culture and immunocytochemistry* : Monkey kidney fibroblasts (COS-7 cell-line, ATCC) were cultured at  $37^\circ C$  and 5% CO<sub>2</sub> in DMEM (Welgene) supplemented with 10% FBS (Thermo Fisher Scientific). For immunocytochemistry, cells were fixed in 4% formaldehyde, 4% sucrose, PBS for 15 minutes, permeabilized for 5 min in 0.25% Triton X-100, PBS and blocked for 30 min in 10% BSA, PBS at  $37^\circ C$ . The cells were incubated with Tubulin antibody (AbCam), 3% BSA, PBS for 2 hours at  $37^\circ C$ , washed in PBS, and incubated with Alexa-488 secondary antibody (Thermo Fisher Scientific), 3% BSA, PBS for 45 min at  $37^\circ C$ .

2) *Epifluorescence Microscopy*: For three-dimensional epifluorescence microscopy, samples were mounted on a coverglass and imaged using N-SIM based on an inverted microscope (ECLIPSE Ti-E, NIKON), equipped with an oil immersion objective lens (Apo TIRF 100x, N.A. 1.49, NIKON) and an EMCCD camera (iXon DU-897, Andor Technology). The acquired datasets were comprised of 50 axial sections of  $512 \times 512$  pixels. The voxel size of the reconstructed images was 64 nm in the x- and y-dimensions and 60 nm in the z-dimension, with 16-bit depth.

### C. Network training

A total 18 EPF samples of tubulin with a size of  $512 \times 512 \times 30$  were used for training, and one for validation. As for unmatched sharp image volume, we used deblurred image generated by utilizing a commercial software AutoQuant X3 (Media Cybernetics, Rockville). The EPF volume depth was increased to 64 using the reflection boundary condition. Due to GPU memory limitations, the EPF volume was split into  $64 \times 64 \times 64$  size patches.

For data augmentation, rotation, flip, translation, and scale were imposed on the input patches. We normalized the patches and set them to [0,1]. Adam optimizer [31] was also used for training. The learning rate was initially set to 0.0001, which is decreased linearly after 40 epoch, and the total number of epoch was 200 epoch. For the optimizer, we used only a single batch.

To reduce model oscillation [10], the discriminators used a history of generated volumes from a frame buffer containing 50 previously generated volumes, as described in [32].

The proposed method was implemented in Python with Tensorflow, and GeForce GTX 1080 Ti GPU was used for both training and testing the network.

### D. Baseline algorithms

To verify the performance of the proposed method, we compare our method with a supervised learning network, the conventional cycleGAN with two deep generators [18], and the commercial deconvolution method using AutoQuant X3 (Medical Cybernetics, Rockville). For a supervised learning network, we trained a 3D U-net with the ground-truth data

for the case of simulation study, and the matched label data from AutoQuant X3 for the case of real microscopy data set. All the reconstruction results were post-processed for better visualization by adaptive histogram equalization [33].

### E. Performance Metrics

In the simulation study, the ground-truth data are available, so we validated our model quantitatively using the peak signal-to-noise ratio (PSNR) and structural similarity index metric (SSIM) [34]. The PSNR is defined as follows:

$$MSE = \frac{1}{N_x N_y} \sum_{i=0}^{N_x-1} \sum_{j=0}^{N_y-1} [x(i, j) - \hat{x}(i, j)]^2$$

$$PSNR = 10 \log_{10} \left( \frac{MAX_x^2}{MSE} \right)$$

where  $N_x$  and  $N_y$  are x- and y- dimension of the ground-truth image  $x$ ,  $\hat{x}$  is the noisy image approximation,  $MAX_x$  is the maximum possible pixel value of the image. The SSIM is defined as follows:

$$SSIM(x, \hat{x}) = \frac{(2\mu_x \mu_{\hat{x}} + c_1)(2\sigma_{x\hat{x}} + c_2)}{(\mu_x^2 + \mu_{\hat{x}}^2 + c_1)(\sigma_x^2 + \sigma_{\hat{x}}^2 + c_2)}$$

where  $\mu$  is the average of the image,  $\sigma_x, \sigma_{\hat{x}}$  is the variance of the images  $x$  and  $\hat{x}$ ,  $\sigma_{x\hat{x}}$  is the covariance of the images,  $c_1 = (k_1, L)^2$  and  $c_2 = (k_2, L)^2$  are the variables to stabilize the division with weak denominator where  $L$  is a dynamic range of the pixel intensities, and  $k_1 = 0.01$  and  $k_2 = 0.03$  by default.

## VI. EXPERIMENTAL RESULTS

### A. Simulation Results

Fig. 5 shows qualitative comparisons of different reconstruction methods over datasets generated by the theoretical PSFs at different wavelengths. Here, the training was performed using the blurred data with  $\lambda = 500$ nm PSF kernel, but the inference was performed using data with wavelength 400 nm, 500 nm, and 600 nm, respectively. The goal of this study is to investigate the generalization power of the proposed method with respect to different wavelengths.

The supervised method removed most blur and noise; however, it lost many fine details of the tubule structure and showed false continuity over the tubule structure. The conventional cycleGAN method showed better qualitative results than the supervised one, presenting finer details and the correct continuity of the tubule structure, but still some of the structures were not fully recovered. On the other hand, the proposed method showed the best qualitative results, recovering most of the microtubule structures. Moreover, as shown in Table I, the proposed method showed the best PSNR and SSIM scores. This confirmed that the proposed method generalizes well, even when the PSF model for the training data is not matched well with that of the inference phase.

In the next experiment, we evaluated the proposed cycleGAN approaches in a non-blind deconvolution set-up, where the blur kernel  $h(r)$  is known. In this case, the estimation of  $h$  is no more necessary in (22) so that one may wonder whether



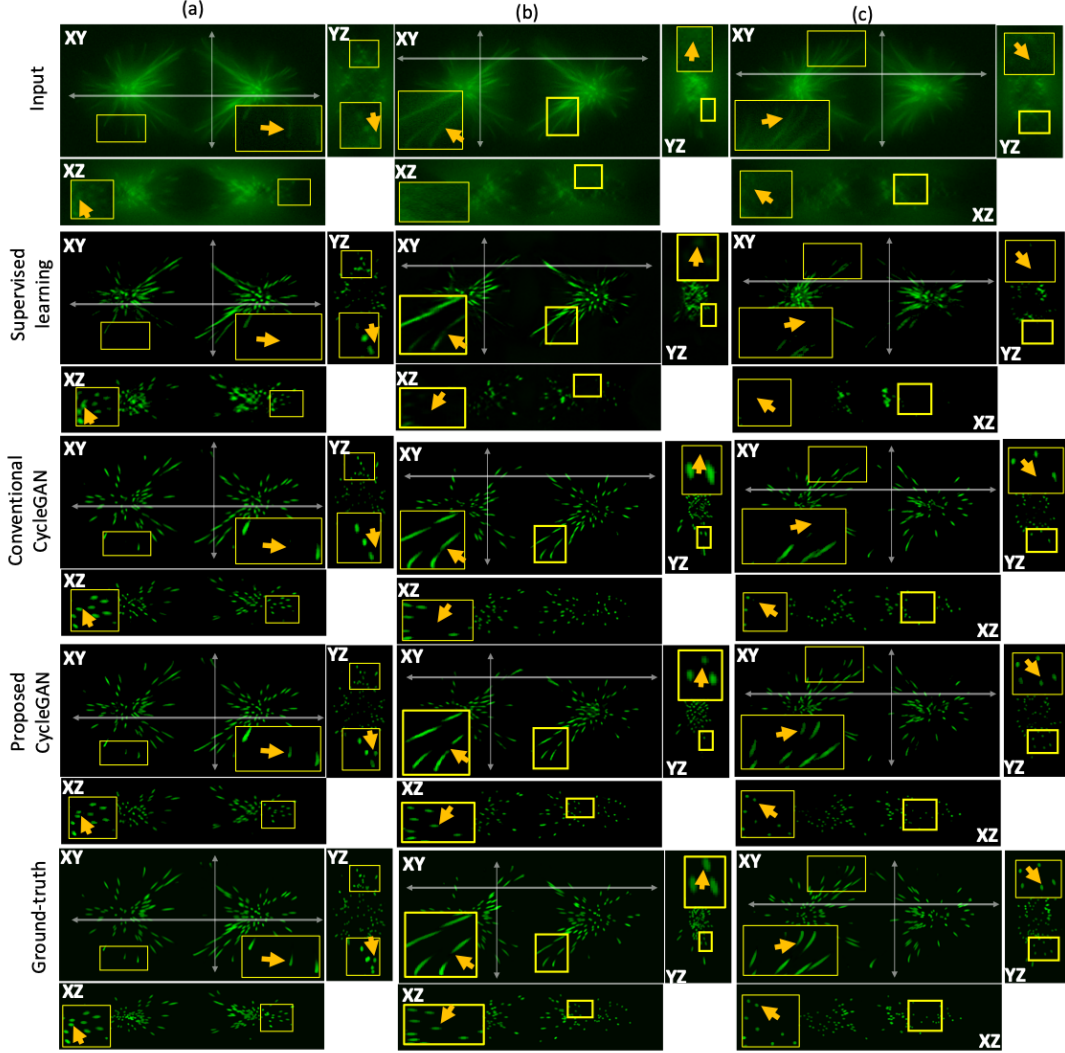


Fig. 5: Generalization performance comparison of various methods. The following parameters were used for the training and inference:  $NA = 1.4$ ,  $n_i = 1.5$ , and  $\sigma = 3$ ,  $m = 7$ . For the training data, the wavelength was  $\lambda = 500nm$ . (a) Reconstruction result at the inference phase using the data with  $\lambda = 400nm$ . (b) Reconstruction result at the inference phase using the data with  $\lambda = 500nm$ . (c) Reconstruction result at the inference phase using the data with  $\lambda = 600nm$ . Two different views (YZ, XZ) were displayed along the corresponding lines. The ROIs (marked yellow) show the area for the enlarged parts.

		PSNR (dB)	SSIM
(a)	Input	18.1087	0.5651
	Supervised learning	25.6607	0.9209
	Conventional CycleGAN	25.7616	0.9444
	Proposed CycleGAN	<b>26.4960</b>	<b>0.9513</b>
(b)	Input	17.8018	0.5201
	Supervised learning	25.4048	0.9162
	Conventional CycleGAN	25.5837	0.9410
	Proposed CycleGAN	<b>26.2891</b>	<b>0.9480</b>
(c)	Input	17.5045	0.4929
	Supervised learning	25.1191	0.9113
	Conventional CycleGAN	25.3379	0.9369
	Proposed CycleGAN	<b>26.0044</b>	<b>0.9437</b>

TABLE I: Generalization performance comparison of various methods of Fig. 5 in terms of PSNR and SSIM.

the use of one-branch of the proposed cycleGAN (what we call “half cycleGAN”) may suffice, so we also evaluated the results

from such architecture.

Fig. 6 compares the reconstruction results by various implementations of the proposed method. In Fig. 6(a), the input image at the inference phase was generated by assuming wavelength  $\lambda = 500nm$ . Although all the reconstruction results by various methods showed nice details of the structure, our non-blind cycleGAN approach resulted in the best PSNR and SSIM score as shown in Table II. Interestingly, our blind cycleGAN approach that estimates both blur kernel  $h$  and the image  $f$  provides slightly better results than the non-blind counterpart. On the other hand, half cycleGAN approach results in the inferior performance. In Fig. 6(b), the input image is more blurry than (a) due to the longer wavelength  $\lambda = 610nm$ . Our blind cycleGAN approach was slight better than our non-blind cycleGAN approach in terms of PSNR values, although the SSIM score is still better for the non-blind approach. On the

		PSNR (dB)	SSIM
(a)	Input	17.8018	0.5201
	Non-blind CycleGAN	25.8754	0.9291
	Half CycleGAN	24.8256	0.9093
	Blind CycleGAN	<b>26.2891</b>	<b>0.9480</b>
(b)	Input	17.4477	0.4863
	Non-blind CycleGAN	25.5512	<b>0.9229</b>
	Half CycleGAN	24.8861	0.9106
	Blind CycleGAN	<b>25.6355</b>	0.9148

TABLE II: Non-blind deconvolution performance comparison of various implementation of the proposed method (see Fig. 6) in terms of PSNR and SSIM.

other hand, half cycleGAN approaches again produced inferior results. These results clearly indicates that our cycleGAN approach is very robust even when the exact PSF is unknown, by providing nearly similar results as non-blind cycleGAN approach.

### B. Real Epifluorescence Microscopy Data

Fig. 7 show lateral and sagittal views of reconstruction results by various methods. In Fig. 7, input images are degraded by blur and noises. Besides, as shown in the sagittal views, the degradation at deeper area gets worse. In Fig. 7, AutoQuant X3 removed blur and noise; however, it did not improve contrast sufficiently. The supervised learning and the standard cycleGAN with two generators showed better contrast and removed blur; however, the structural continuity was not preserved. On the other hand, in our cycleGAN approaches, blurs and noise were successfully removed, thereby preserving the continuity of the structure.

### C. Computational time

The training time for the proposed network was 10 hours for the simulation study, and 18 hours for the real microscopy experiments, respectively. At inference phase, the computational time for  $256 \times 512 \times 128$  volume image in the simulation study was 18.9sec, and it was 15sec for  $512 \times 512 \times 50$  size volume for the real microscopy experiments.

## VII. CONCLUSIONS

In this paper, we presented a novel cycleGAN architecture with a linear blur kernel for deconvolution microscopy, which can be used for both non-blind and blind deconvolution problems in an unsupervised manner. In contrast to the existing cycleGAN approaches with two CNN-based generators, in the proposed method only a single CNN-based generator is necessary to convert the low resolution image to high resolution one, whereas the blur image is generated using a simple linear layer. We showed that the proposed architecture is indeed a dual formulation of an optimal transport problem that uses the penalized least squares cost as the transport cost between two measures supported on low- and high-resolution image manifold. This stabilized the inverse solution by exploiting the similarity of two measures in the low and high resolution image manifolds.

We used the synthetic microtubule network and the real epi-fluorescent microscopy data to validate our model. In both

non-blind and blind setups, the proposed method accurately reconstructed high resolution images, which were better than the existing methods. Moreover, our experimental results showed that our method generalized well for the deconvolution problems from different PSFs.

Given the robustness and the fast computational time, we believe that our method can be an important platform for deconvolution microscopy.

## APPENDIX

Although mathematical proof can be found in our companion paper [35], we include it here to make the paper self-contained.

First, from the definition of  $\ell_{cycle}$  and  $\ell_{OT'}$  in (16) and (18), it is straightforward to show that

$$\mathbb{T}(\Theta, \mathcal{H}) \geq \ell_{cycle}(\Theta, \mathcal{H}) + \ell_{OT'}(\Theta, \mathcal{H}). \quad (24)$$

To show that the inequality becomes the equality, we need the classical results on optimal transport for the restricted measure [12]. Specifically, [12, Theorem 4.6, p.46] informs that for some optimal transportation plan  $\pi^*$ , the restrictions  $\pi^*|_{A \cup B}$  and  $\pi^*|_{\mathcal{X} \times \mathcal{Y} \setminus (A \cup B)}$  inherit the optimality. Therefore,

$$\begin{aligned} \mathbb{T}(\Theta, \mathcal{H}) &= \int_{\mathcal{X} \times \mathcal{Y}} c(x, y; \Theta, \mathcal{H}) d\pi^*(x, y) \\ &= \int_{A \cup B} c(x, y; \Theta, \mathcal{H}) d\pi^*(x, y) \\ &\quad + \int_{\mathcal{X} \times \mathcal{Y} \setminus (A \cup B)} c(x, y; \Theta, \mathcal{H}) d\pi^*(x, y) \\ &= \ell_{cycle}(\Theta, \mathcal{H}) + \ell_{OT'}(\Theta, \mathcal{H}) \end{aligned}$$

This achieves the upper bound in (24).

Second, by virtue of the definitions of the cost function and the sets  $A$  and  $B$ , we have

$$c(x, y; \Theta, \mathcal{H}) = \|y - \mathcal{H}G_{\Theta}(y)\|^q \text{ on } A,$$

$$c(x, y; \Theta, \mathcal{H}) = \|x - G_{\Theta}(\mathcal{H}x)\|^p \text{ on } B,$$

$$c(x, y; \Theta, \mathcal{H}) = 0 \quad \text{on } A \cap B.$$

Hence,

$$\begin{aligned} \int_{A \cup B} c(x, y; \Theta, \mathcal{H}) d\pi^*(x, y) &= \int_B \|x - G_{\Theta}(\mathcal{H}x)\|^p d\pi^*(x, y) \\ &\quad + \int_A \|y - \mathcal{H}G_{\Theta}(y)\|^q d\pi^*(x, y) \end{aligned}$$

Furthermore, we use the disintegration theorem [36] to split the joint measure  $\pi^*$  as follows:

$$d\pi^*(x, y) = \pi^*(dy|x)\mu(dx) = \pi^*(dx|y)\nu(dy),$$

where  $\pi^*(\mathcal{Y}|x) = 1$   $\mu$ -a.e. and  $\pi^*(\mathcal{X}|y) = 1$   $\nu$ -a.e. Then, we have

$$\int_B \|x - G_{\Theta}(\mathcal{H}x)\|^p d\pi^*(x, y)$$



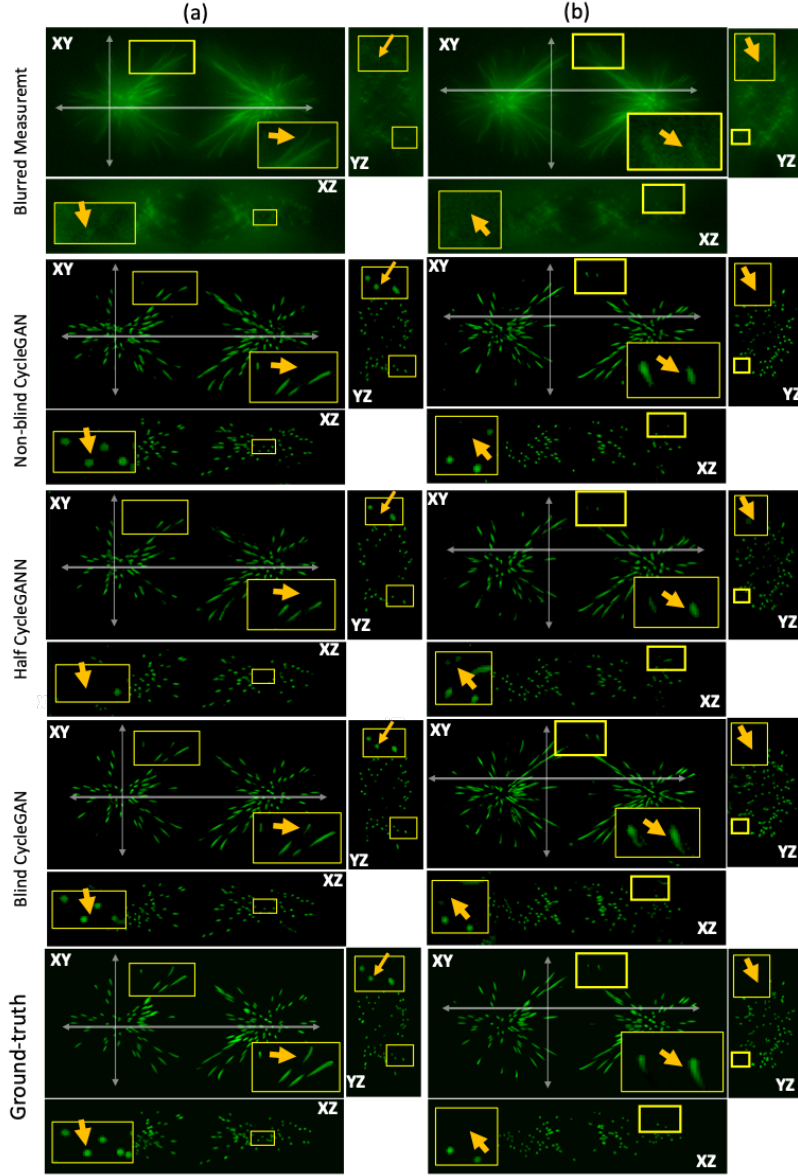


Fig. 6: Deconvolution performance of various implementation of the proposed approach when the PSF is known. Non-blind cycleGAN uses the available PSF for a blur generator, and half cycleGAN uses the top cycle of Fig. 2 with the known blur kernel. The proposed blind cycleGAN estimates both PSF and the image. The following parameters were used for the training and inference:  $NA = 1.4$ ,  $n_i = 1.5$ ,  $\sigma = 3$ ,  $m = 7$ . (a) Reconstruction results using the training/inference data using  $\lambda = 500nm$ . (b) Reconstruction resulting using the training/inference data using  $\lambda = 610nm$ . Two different views (YZ, XZ) were displayed along the corresponding lines. The ROIs (marked yellow) show the area for the enlarged parts.

$$\begin{aligned}
&= \int_B \|x - G_\Theta(\mathcal{H}x)\|^p \pi^*(dy|x) \mu(dx) \\
&= \int_{\mathcal{X}} \int_{y=\mathcal{H}x} \|x - G_\Theta(\mathcal{H}x)\|^p \pi^*(dy|x) \mu(dx) \\
&= \int_{\mathcal{X}} \|x - G_\Theta(\mathcal{H}x)\|^p \int \mathbf{1}_{y=\mathcal{H}x} \pi^*(dy|x) \mu(dx) \\
&= \int_{\mathcal{X}} \|x - G_\Theta(\mathcal{H}x)\|^p \rho(x) \mu(dx)
\end{aligned}$$

$\int \mathbf{1}_{x=G_\Theta(y)} \pi^*(dx|y)$ , we have

$$\int_A c(x, y; \Theta, \mathcal{H}) d\pi^*(x, y) = \int_Y \|y - \mathcal{H}G_\Theta(y)\|^q \sigma(y) \nu(dy) .$$

This proves (17).

where  $\mathbf{1}_S$  denotes the indicator function for the set  $S$  and  $\rho(x) = \int \mathbf{1}_{y=\mathcal{H}x} \pi^*(dy|x)$ . In a similar fashion, with  $\sigma(y) =$

Final step of the proof is just a simple corollary of the original Kantorovich's duality formulation proof and the classical results of optimal transport on the restricted measure.

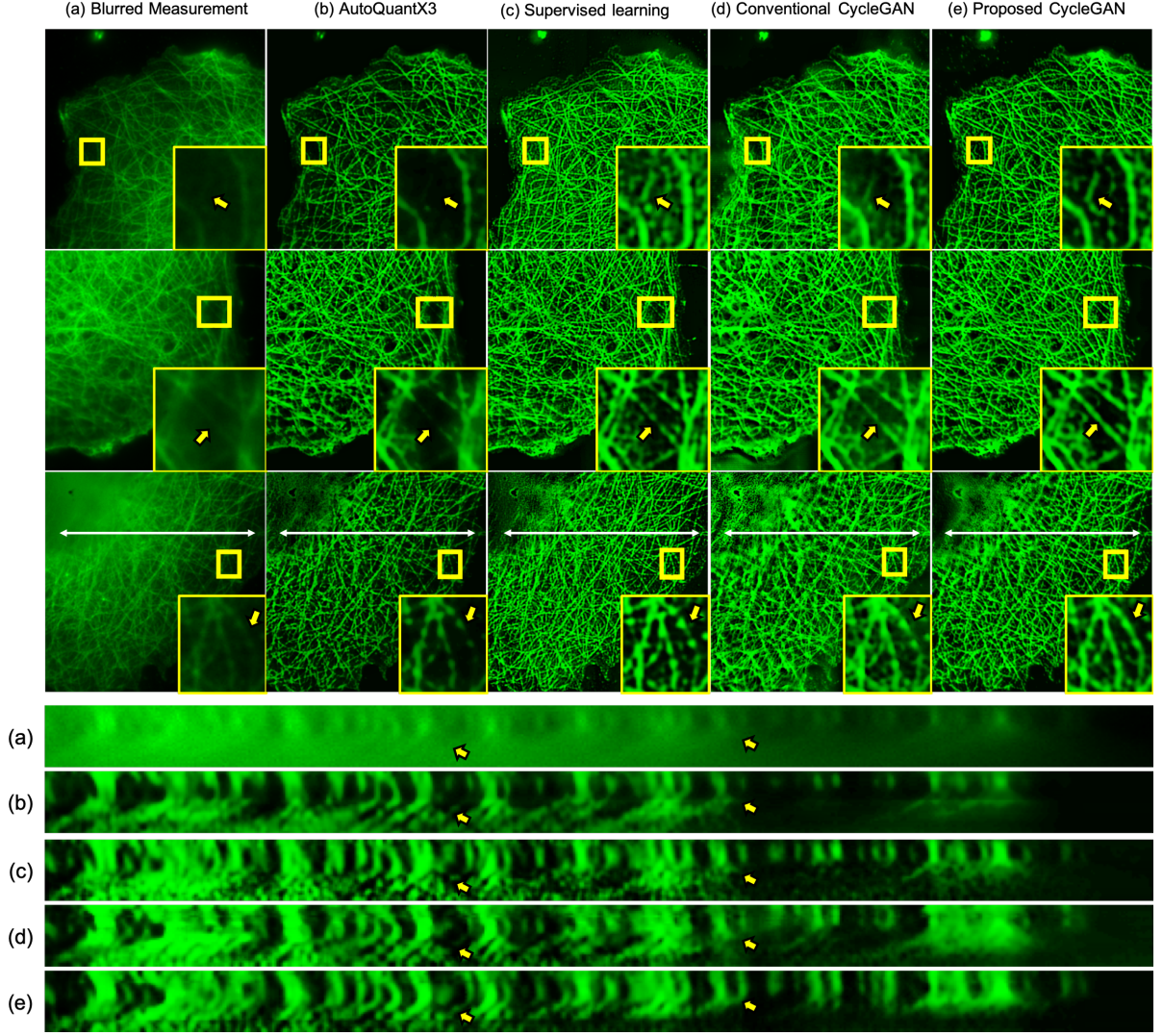


Fig. 7: Comparison of reconstruction results by various methods: (a) Blurred image measurements, (b) AutoQuantX3, (c) supervised learning, (d) the conventional cycleGAN, and (e) the proposed cycleGAN. The ROIs (marked yellow) show the area for the enlarged parts. Sagittal views along the lines in the lateral views.

Specifically, we have

$$\int_{\mathcal{X} \times \mathcal{Y} \setminus (A \cup B)} \|G_{\Theta}(y) - x\|^p \pi^*(dx, dy) = \max_{\varphi} \int_{\mathcal{X}} \varphi(x) \mu'(dx) + \int_{\mathcal{Y}} \varphi^c(G_{\Theta}(y)) \nu'(dy)$$

where  $\mu'$  and  $\nu'$  are marginals of the restriction of optimal transportation plan on the restricted set  $\mathcal{X} \times \mathcal{Y} \setminus (A \cup B)$ . Now, using Proposition 3 in our companion paper [35], we have

$$\begin{aligned} & \int_{\mathcal{X} \times \mathcal{Y} \setminus (A \cup B)} \|G_{\Theta}(y) - x\| \pi^*(dx, dy) \\ &= \max_{\varphi} \int_{\mathcal{X}} \varphi(x) \mu(dx) + \int_{\mathcal{Y}} \varphi^c(G_{\Theta}(y)) \nu(dy) \\ &= \max_{\varphi} \int_{\mathcal{X}} \varphi(x) \mu(dx) - \int_{\mathcal{Y}} \varphi(G_{\Theta}(y)) \nu(dy) \end{aligned}$$

for the non-restricted marginals  $\mu$  and  $\nu$ , where for the last equality we use  $\varphi^c = -\varphi$  for  $p = 1$  when  $\varphi$  is 1-Lipschitz [12]. Using the same technique, the second term in (18) can be equivalently represented as

$$\begin{aligned} & \int_{\mathcal{X} \times \mathcal{Y} \setminus (A \cup B)} \|y - \mathcal{H}x\| d\pi(x, y) \\ &= \max_{\psi} \int_{\mathcal{Y}} \psi(y) d\nu(y) - \int_{\mathcal{X}} \psi(\mathcal{H}x) d\nu(x), \end{aligned}$$

where  $\psi$  is 1-Lipschitz. By collecting terms, we prove (19). This concludes the proof.

#### ACKNOWLEDGMENT

This work is supported by National Research Foundation of Korea (Grant NRF-2016R1A2B3008104 and NRF-2017M3C7A1047904).

## REFERENCES

- [1] P. Sarder and A. Nehorai, "Deconvolution methods for 3-D fluorescence microscopy images," *IEEE Signal Processing Magazine*, vol. 23, no. 3, pp. 32–45, 2006.
- [2] S. Chaudhuri, R. Velmurugan, and R. Rameshan, "Blind deconvolution methods: A review," in *Blind Image Deconvolution*. Springer, 2014, pp. 37–60.
- [3] J. G. McNally, T. Karpova, J. Cooper, and J. A. Conchello, "Three-dimensional imaging by deconvolution microscopy," *Methods*, vol. 19, no. 3, pp. 373–385, 1999.
- [4] Y.-L. You and M. Kaveh, "A regularization approach to joint blur identification and image restoration," *IEEE Transactions on Image Processing*, vol. 5, no. 3, pp. 416–428, 1996.
- [5] T. F. Chan and C.-K. Wong, "Total variation blind deconvolution," *IEEE transactions on Image Processing*, vol. 7, no. 3, pp. 370–375, 1998.
- [6] Y. Rivenson, Z. Göröcs, H. Günaydin, Y. Zhang, H. Wang, and A. Ozcan, "Deep learning microscopy," *Optica*, vol. 4, no. 11, pp. 1437–1443, 2017.
- [7] E. Nehme, L. E. Weiss, T. Michaeli, and Y. Shechtman, "Deep-STORM: super-resolution single-molecule microscopy by deep learning," *Optica*, vol. 5, no. 4, pp. 458–464, 2018.
- [8] M. Weigert, L. Royer, F. Jug, and G. Myers, "Isotropic reconstruction of 3D fluorescence microscopy images using convolutional neural networks," in *International Conference on Medical Image Computing and Computer-Assisted Intervention*. Springer, 2017, pp. 126–134.
- [9] P. Zelger, K. Kaser, B. Rossboth, L. Velas, G. Schütz, and A. Jesacher, "Three-dimensional localization microscopy using deep learning," *Optics express*, vol. 26, no. 25, pp. 33 166–33 179, 2018.
- [10] I. Goodfellow, J. Pouget-Abadie, M. Mirza, B. Xu, D. Warde-Farley, S. Ozair, A. Courville, and Y. Bengio, "Generative adversarial nets," in *Advances in neural information processing systems*, 2014, pp. 2672–2680.
- [11] M. Arjovsky, S. Chintala, and L. Bottou, "Wasserstein GAN," *arXiv preprint arXiv:1701.07875*, 2017.
- [12] C. Villani, *Optimal transport: old and new*. Springer Science & Business Media, 2008, vol. 338.
- [13] G. Peyré, M. Cuturi *et al.*, "Computational optimal transport," *Foundations and Trends in Machine Learning*, vol. 11, no. 5-6, pp. 355–607, 2019.
- [14] T. Nguyen, Y. Xue, Y. Li, L. Tian, and G. Nehmetallah, "Deep learning approach for Fourier ptychography microscopy," *Optics express*, vol. 26, no. 20, pp. 26 470–26 484, 2018.
- [15] O. Kupyn, V. Budzan, M. Mykhailych, D. Mishkin, and J. Matas, "Deblurgan: Blind motion deblurring using conditional adversarial networks," in *Proceedings of the IEEE Conference on Computer Vision and Pattern Recognition*, 2018, pp. 8183–8192.
- [16] J.-Y. Zhu, T. Park, P. Isola, and A. A. Efros, "Unpaired image-to-image translation using cycle-consistent adversarial networks," in *Proceedings of the IEEE international conference on computer vision*, 2017, pp. 2223–2232.
- [17] E. Kang, H. J. Koo, D. H. Yang, J. B. Seo, and J. C. Ye, "Cycle-consistent adversarial denoising network for multiphase coronary CT angiography," *Medical physics*, vol. 46, no. 2, pp. 550–562, 2019.
- [18] Y. Lu, Y.-W. Tai, and C.-K. Tang, "Conditional cyclegan for attribute guided face image generation," *arXiv preprint arXiv:1705.09966*, 2017.
- [19] J. Adler, A. Ringh, O. Öktem, and J. Karlsson, "Learning to solve inverse problems using Wasserstein loss," *arXiv preprint arXiv:1710.10898*, 2017.
- [20] J. Zhang, J. Pan, W.-S. Lai, R. W. Lau, and M.-H. Yang, "Learning fully convolutional networks for iterative non-blind deconvolution," in *Proceedings of the IEEE Conference on Computer Vision and Pattern Recognition*, 2017, pp. 3817–3825.
- [21] H. K. Aggarwal, M. P. Mani, and M. Jacob, "MoDL: Model-based deep learning architecture for inverse problems," *IEEE transactions on medical imaging*, vol. 38, no. 2, pp. 394–405, 2018.
- [22] M.-Y. Liu, T. Breuel, and J. Kautz, "Unsupervised image-to-image translation networks," in *Advances in neural information processing systems*, 2017, pp. 700–708.
- [23] Z. Yi, H. Zhang, P. Tan, and M. Gong, "Dualgan: Unsupervised dual learning for image-to-image translation," in *Proceedings of the IEEE international conference on computer vision*, 2017, pp. 2849–2857.
- [24] D. Lee, J. Kim, W.-J. Moon, and J. C. Ye, "CollaGAN: Collaborative GAN for missing image data imputation," in *Proceedings of the IEEE Conference on Computer Vision and Pattern Recognition*, 2019, pp. 2487–2496.
- [25] B. Kim, J. Kim, J.-G. Lee, D. H. Kim, S. H. Park, and J. C. Ye, "Unsupervised deformable image registration using cycle-consistent CNN," *arXiv preprint arXiv:1907.01319*, 2019.
- [26] Ö. Çiçek, A. Abdulkadir, S. S. Lienkamp, T. Brox, and O. Ronneberger, "3D U-Net: learning dense volumetric segmentation from sparse annotation," in *International conference on medical image computing and computer-assisted intervention*. Springer, 2016, pp. 424–432.
- [27] D. Ulyanov, A. Vedaldi, and V. Lempitsky, "Instance normalization: The missing ingredient for fast stylization," *arXiv preprint arXiv:1607.08022*, 2016.
- [28] P. Isola, J.-Y. Zhu, T. Zhou, and A. A. Efros, "Image-to-image translation with conditional adversarial networks," in *Proceedings of the IEEE conference on computer vision and pattern recognition*, 2017, pp. 1125–1134.
- [29] D. Sage, L. Donati, F. Soulez, D. Fortun, G. Schmit, A. Seitz, R. Guiet, C. Vonesch, and M. Unser, "DeconvolutionLab2: An open-source software for deconvolution microscopy," *Methods*, vol. 115, pp. 28–41, 2017.
- [30] H. Kirshner, D. Sage, and M. Unser, "3D PSF models for fluorescence microscopy in ImageJ," in *Proceedings of the Twelfth International Conference on Methods and Applications of Fluorescence Spectroscopy, Imaging and Probes (MAF'11)*, vol. 154, 2011.
- [31] D. P. Kingma and J. Ba, "Adam: A method for stochastic optimization," *arXiv preprint arXiv:1412.6980*, 2014.
- [32] A. Shrivastava, T. Pfister, O. Tuzel, J. Susskind, W. Wang, and R. Webb, "Learning from simulated and unsupervised images through adversarial training," in *Proceedings of the IEEE conference on computer vision and pattern recognition*, 2017, pp. 2107–2116.
- [33] S. M. Pizer, E. P. Amburn, J. D. Austin, R. Cromartie, A. Geselowitz, T. Greer, B. ter Haar Romeny, J. B. Zimmerman, and K. Zuiderveld, "Adaptive histogram equalization and its variations," *Computer vision, graphics, and image processing*, vol. 39, no. 3, pp. 355–368, 1987.
- [34] Z. Wang, A. C. Bovik, H. R. Sheikh, E. P. Simoncelli *et al.*, "Image quality assessment: from error visibility to structural similarity," *IEEE transactions on image processing*, vol. 13, no. 4, pp. 600–612, 2004.
- [35] B. Sim, G. Oh, S. Lim, and J. C. Ye, "Optimal transport, CycleGAN, and penalized LS for unsupervised learning in inverse problems," *arXiv preprint arXiv:1909.12116*, 2019.
- [36] D. Simmons, "Conditional measures and conditional expectation; rohlin's disintegration theorem," *Discrete & Continuous Dynamical Systems-A*, vol. 32, no. 7, pp. 2565–2582, 2012.